Advanced Materials Technologies, Volume 9, Issue 10, May 2024, Article number 2302075
DOI: 10.1002/admt.202302075

Fast emitting nanocomposites for high-resolution ToF-PET imaging based on multicomponent scintillators.

*Matteo Orfano, Fiammetta Pagano, Ilaria Mattei, Francesca Cova, Valeria Secchi, Silvia Bracco, Edith Rogers, Luca Barbieri, Roberto Lorenzi, Gregory Bizarri, Etiennette Auffray, Angelo Monguzzi**

M. Orfano, F. Cova, V. Secchi, L. Barbieri, S. Bracco, R. Lorenzi, A. Monguzzi
Dipartimento di Scienza dei Materiali, Università degli Studi Milano-Bicocca, via R. Cozzi 55, 20125 Milano, Italy
E-mail: angelo.monguzzi@unimib.it

V. Secchi, A. Monguzzi
NANOMIB, Center for Biomedical Nanomedicine, University of Milano-Bicocca, 20126 Milan, Italy

F. Pagano, E. Auffray
CERN, Geneva, Switzerland.

F. Pagano
Dipartimento di Fisica Giuseppe Occhialini, Università degli Studi Milano Bicocca, Piazza della Scienza 3, 20126 Milano

E. Rogers, G. Bizarri
Cranfield University, School of Aerospace, Transport & Manufacturing, MK43 0AL, UK

I. Mattei
INFN Sezione di Milano, via G. Celoria 16, 20133, Milan, Italy

Keywords: scintillation, nanocomposites, ToF-PET, energy sharing, optical device, conjugated chromophores, multicomponent scintillators.

Abstract. Time-of-Flight Positron Emission Tomography is a medical imaging technique, based on the detection of two back-to-back γ-photons generated from radiotracers injected in the body. Its limit is the ability of employed scintillation detectors to discriminate in time the arrival of γ-pairs, i.e. the coincidence time resolution (*CTR*). A *CTR* < 50 ps that would enable fast imaging with ultralow radiotracer dose. Monolithic materials do not have simultaneously the required high light output and fast emission characteristics, thus the concept of scintillating heterostructure is proposed, where the device is made of a dense scintillator coupled to a fast-emitting light material. Here we present a composite polymeric scintillator loaded with hafnium oxide nanoparticles. This enhanced by +300% its scintillation yield, surpassing commercial plastic scintillators. The nanocomposite is coupled to bismuth germanate oxide (BGO) realizing a multilayer metascintillator. We observed the energy sharing between its components, which activate the nanocomposite fast emission enabling a net *CTR* improvement of 25% with respect to monolithic BGO. These results demonstrate that a controlled loading with dense nanomaterials is an excellent strategy to enhance the performance of polymeric scintillators for their use in advanced radiation detection and imaging technologies.

Published by Wiley. This is the Author Accepted Manuscript issued with: Creative Commons Attribution Non-Commercial License (CC:BY:NC 4.0).
The final published version (version of record) is available online at DOI:10.1002/admt.202302075. Please refer to any applicable publisher terms of use.

1. Introduction

Time-of-Flight Positron Emission Tomography (ToF-PET) is a powerful imaging technique that provide reliable information in a variety of medical fields, from oncology to neurology.[1] Briefly, a radiotracer labelled with a β- radioactive isotope (a positron emitter) is injected into the patient and then it is attracted to areas of increased metabolic activity, such as tumours. The isotope undergoes radioactive decay, releasing a positron that annihilates with a surrounding electron producing two back-to-back γ photons with 511 keV energy. As showed in **Figure 1a**, these γ-rays are sensed by scintillating detectors placed around the patient's body. The recorded signals are therefore used to reconstruct the image of the radio-labelled tissue. One of the limiting factors of this technique is the detectors ability to discriminate in time the arrival of the back-to-back γ-photons pairs. The uncertainty on the position Δx of the annihilation event along the back-to-back line of response is given by

$$\Delta x = \frac{c\Delta t}{2}, \qquad \text{Eq. 1}$$

where c is the speed of light in vacuum and $\Delta t = t_2 - t_1$ is the uncertainty on the different detection times of the two γ photons, i.e. the coincidence time resolution (CTR, Fig.1b).[2] The CTR is therefore a crucial figure of merit for a ToF-PET detector. Using monolithic scintillators, it can be estimated from several parameters intrinsic of the material as

$$CTR = 3.33\left(\frac{\tau_{rise}\tau_{eff}}{N}\right)^{0.5} = 3.33\left(\frac{\tau_{rise}\tau_{eff}}{\beta\chi[\Phi_{scint}E]}\right)^{0.5}, \qquad \text{Eq. 2}$$

where $\tau_{rise} = (1.57\tau^0_{rise} - 1.15\tau_{opt})$ is the global scintillation pulse rise time constant given by the intrinsic scintillation rise time τ^0_{rise} of the material plus the average optical photon transit time in the device to the photodetector τ_{opt}.[3] The effective emission time $\tau_{eff} = (k_{dtc})^{-1}$ is the reciprocal of the detection rate of scintillation photons k_{dtc} (Supporting Information, section 1). N represent the absolute light output, i.e. the number of photons collected by the photodetector. The light output can be expressed as function of several parameters specific of any scintillator, including the amount of energy deposited in the scintillator E, the scintillator light yield Φ_{scint} that indicate the number of photons generated per MeV of deposited energy, the light outcoupling efficiency β that set the fraction of scintillation photons that reach the photodetector, and the photodetector quantum efficiency χ.

As suggested by Eq. 1, the CTR should be as low as possible to improve the instrument sensitivity and the image signal-to-noise ratio at low radiotracers concentration,[4] thus potentially allowing a broad use of safe, low-dose and fast ToF-PET screening protocols and opening the way also to yet unexplored application in neurology and paediatrics. State-of-the-art commercial machines works with CTR = 210 ps, [5] so much effort is then put in the development of new scintillators aiming at a CTR of 10 ps that would allow fast imaging with acquisition times shorter with respect to the standard clinical using very low limited radiotracer dose.[6] Unfortunately, none of the existing monolithic scintillators shows simultaneously the high Φ_{scint} and the sub-nanosecond τ_{eff} necessary to reach the 10 ps CTR. High Φ_{scint} are typical of slow emitting heavy crystals,[7] while organic and plastic scintillators have fast emission also in the sub-nanosecond range[8] but a low density inadequate to stop the 511 keV γ-rays in the small ToF-PET detectors architecture.

In order to overcome this obstacle, the concept of scintillating heterostructure has been proposed.[9][10] Here the scintillator is fabricated by coupling heavy crystalline scintillators, such as the bismuth germanate oxide (BGO), to fast-emitting plastic scintillators realizing a multicomponent device (Fig.1c). The dense component stops γ-rays by means of photoelectric effect, thus enabling the selection of the correct back-to-back 511 keV events. The fast emission is activated directly by charges recombination and, importantly, by the energy deposited by diffusing recoil photoelectrons electrons generated in the dense component that reaches the plastic component. This energy sharing mechanism is the key to possibly obtain simultaneously the energy resolution and the sub-200 ps CTR that is required to further improve the quality and speed of the ToF-PET image reconstruction. Unfortunately, organic materials, polymers and plastics have typical densities of $\rho \approx 1$ g cm^{-3}, thus the presence of the fast emitter decreases the global density of the scintillating heterostructure and therefore reduces its effective stopping power at 511 keV.[11]

To mitigate this effect, we developed a composite polymeric fast scintillator whose density was artificially increased by loading it with high density nanoparticles. In particular, we employed polystyrene (PS) as host matrix for the 1,4-bis(5-phenyl-2-oxazolyl)benzene (POPOP) scintillating dye.[12][13] As high density additive, we employed hafnium oxide (HfO_2) nanoparticles because of its high density of $\rho = 9.68$ g cm^{-3}, the feasible synthesis and optical inertness.[14] In an optimized composition, we achieved a 300% improvement of Φ_{scint} surpassing the performance of several commercial plastic scintillators. The nanocomposite has been therefore employed as fast emitting component in the manufacturing of a multilayer heterostructure coupled to crystalline BGO. The prototype device

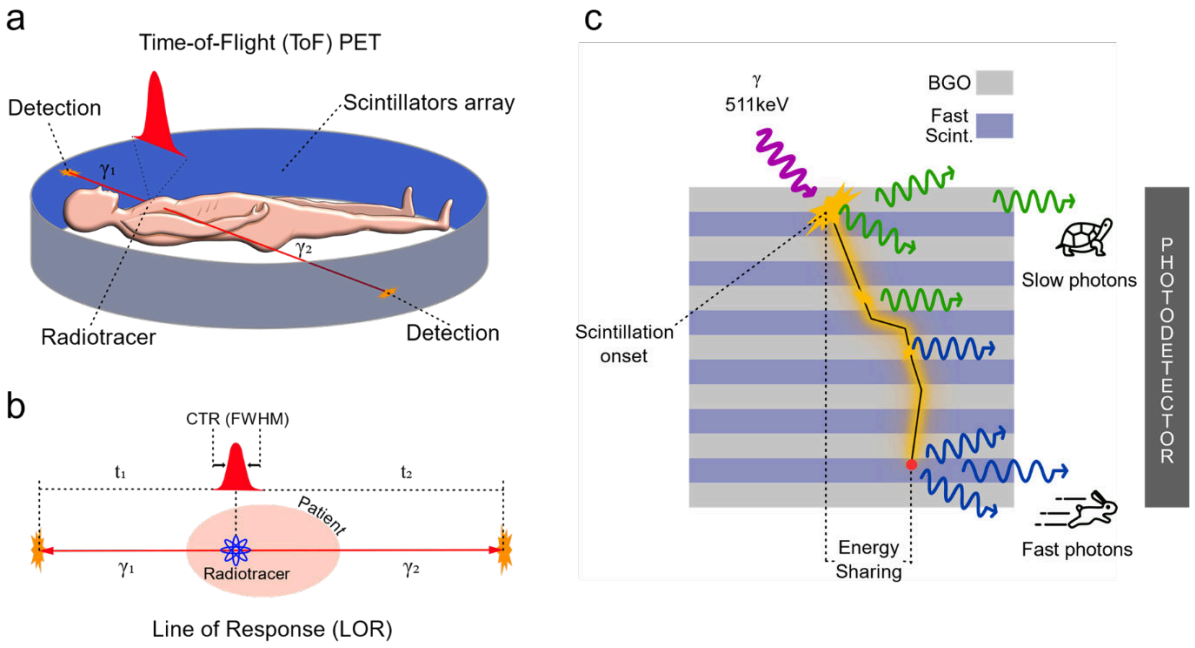

Figure 1. a) Sketch of the basic principles of ToF-PET imaging technique. b) Elements use for the determination of the ToF-PET scanner coincidence time resolution (CTR), which is defined as the average uncertainty Δt of the time difference $t_2 - t_1$ in the detection of the back-to back γ-rays (γ_1 and γ_2) along a selected line of response (LOR) in the detector ring. c) Sketch of the multilayer scintillators built with a series of heterostructure obtained by coupling the heavy scintillating bismuth germanate oxide (BGO) layers and a fast plastic scintillator layer. The fast emission of this latter is activated by exploiting the energy sharing form the photoelectric secondary recoil electrons produce in the BGO upon interaction with the γ-rays.

properties have been investigated by means of photoluminescence and scintillation spectroscopy experiments. We observe the occurrence of energy sharing and a net improvement of the timing performance with respect to the reference monolithic BGO detector. The investigation of the scintillation process kinetics revealed an unexpected deceleration of the nanocomposite fast emission rate due to a still unclear interaction of the guest dye with the host matrix, which partially compensate the achieved gain in the material scintillation yield. The obtained results demonstrate that a controlled loading with dense nanoparticles is an excellent strategy to enhance the Φ_{scint} of plastic scintillators based on fast emitting dyes, as well as the light output of scintillating heterostructures by partially keeping the stopping power required. On the other hand, the spectroscopic analysis performed suggests that a more detailed knowledge and precise control of the excited states interactions during scintillation in the sub-nanosecond time scale are still to be achieved, in order to preserve the dyes emission properties to maximize the device timing performance.

2. Optical and scintillation properties of fast emitting nanocomposites.

Figure 2a sketches out the nanocomposite structure. The PS matrix has been obtained by a thermal-assisted polymerization of styrene monomers, in which POPOP (10^{-2}M) and HfO_2 nanoparticles have been dispersed. The POPOP is a scintillating conjugated chromophore with a photoluminescence quantum yield Φ_{pl}= 0.93 and a photoluminescence lifetime τ_{pl} = 1.4 ns (Fig.S1, Supporting Table S1).[15] As shown in Fig.2b, different processes could lead to visible emission upon interaction of the polymeric matrix with the ionizing radiation.[16] We have both the direct recombination of diffusing charges on the POPOP molecules and the host-guest non radiative energy transfer from the PS matrix to POPOP molecules (Fig.S2). In the proposed composition, 98% of the PS excitons transfer their energy to POPOP molecule with Φ'_{ET} = 1 and an energy transfer rate $k_{ET} \geq 5.6$ GHz = (180 ps)$^{-1}$. The remaining 2% of PS excitons transfer their energy with yield Φ''_{ET} = 0.82 (Supporting Information section 3, Fig.S3). This is ascribed to a slightly non-homogenous dispersion of POPOP molecules. The total energy transfer yield becomes therefore $\Phi_{FS} = 0.98\Phi'_{ET} + 0.02\Phi''_{ET} \approx 1$, observed with both optical or X-rays excitation. The full-organic PS:POPOP sample shows a Φ_{scint} = 3800 ph MeV^{-1} (Methods, Fig.S7). To densify the polymeric scintillator and improve Φ_{scint}, we loaded it with HfO_2 nanoparticles (Methods).[17] The HfO_2 nanoparticles were synthesized by hydrothermal route (Methods, Supplementary Figs. S4-S6).[17] As showed in Fig.2c, the nanoparticles have an oval shape, with size of 85±19 nm and 35±11 nm for the larger and shorter diameter, respectively, which is small enough to not contain the energy deposited by a possible primary interaction with an X-ray, which is properly dispersed in the surrounding polymeric matrix. [18] The nanoparticles show a negligible weak blue emission,[19] thus their primary role remains the enhancement of the interaction with ionizing radiation thanks to the high atomic number of hafnium (Z=72).

A series of scintillating nanocomposites PS:POPOP-xx%wt have been fabricated loading different amounts of nanoparticles (xx%wt) up to 3% in weight (Methods). As shown in Fig.2d, the scintillation intensity and Φ_{scint} progressively increase with the loading level reaching a maximum for the PS:POPOP-2.5%wt sample (inset), with an excellent Φ_{scint} of 9500±475 ph MeV^{-1} that surpasses the 8600 ph MeV^{-1} yield of the reference plastic scintillator EJ-286^{TM} (Fig. S7) or the 8400 ph MeV^{-1} of the EJ-232^{TM}. This composition increases the material density from 1.02 g cm^{-3} to 1.5 g cm^{-3}. ^{13}C solid-state NMR, performed on polystyrene nanocomposites, is a method of choice to highlight the formation of polymer and the absence of residual monomer. Only the characteristic signals of the polymer at 40.7 ppm, 45.9 ppm,

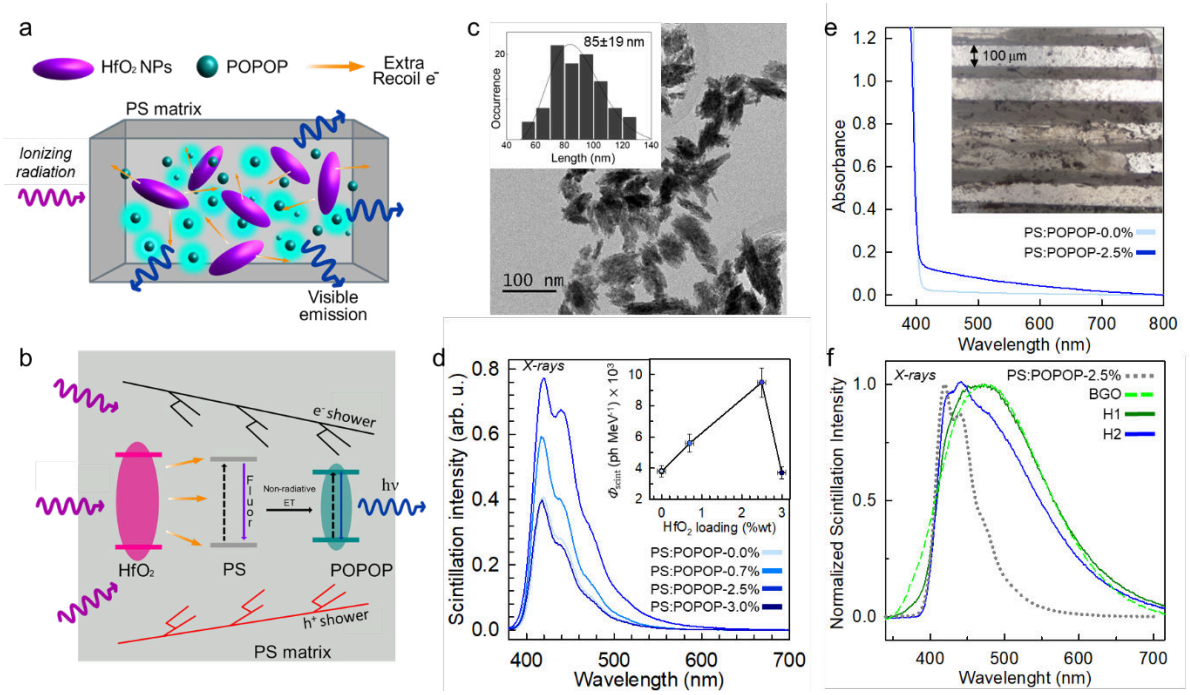

Figure 2. a) Sketch of the multicomponent polystyrene (PS) scintillating nanocomposite loaded with the POPOP dye (10^{-2} M) and HfO_2 nanoparticles (NPs). b) Outline of the photophysics involved in the nanocomposite scintillation process. c) Transmission electron microscopy (TEM) image of NPs. The inset depicts the NPs long axis size distribution obtained by TEM image analysis. The solid line is the fit with a log-normal distribution. d) Scintillation emission spectrum of the nanocomposite PS:POPOP-x% as a function of the NPs loading in weight (%wt) under exposition to soft X-rays. The inset shows the scintillation light yield (Φ_{scint}) measured as function of the loading level. e) Normal incidence optical absorption of 100 µm nanocomposite film with and without the NPs loading (2.5%wt). The inset is digital picture of a 3×3×3 mm^3 multilayer scintillator made of 100 µm BGO and 100 µm nanocomposite alternating layers. f) Scintillation emission spectrum of BGO, PS:POPOP-2.5% and the corresponding single heterostructure under soft X-rays. The heterostructure is excited in two configurations (Fig.S8), by hitting first the BGO (H1) and hitting first the nanocomposite (H2).

128.5 ppm and 146.3 ppm for the CH, CH_2, phenyl-CH and phenyl-C for polystyrene are observed in the ^{13}C CP MAS NMR spectrum (Fig.S9). Further evidence of complete polymerization is provided by differential scanning calorimetric analysis. In fact, the detection of glass transition in the differential scanning calorimetry (DSC) runs at about 97 °C for PS-POPOP-2.5% and 96 °C for PS-POPOP nanocomposites, respectively, suggested that the same degree of polymerization has been reached for both polymeric materials (Fig. S10). Thermogravimetric analyses, performed under oxidative conditions, enabled us to evaluate the thermal stability of polymeric nanocomposites. The degradation process starts at about 350°C for PS-POPOP-2.5% nanocomposite, 25°C much higher than the decomposition temperature of PS-POPOP, indicating the HfO_2 nanoparticles enhance the thermal stability of the polystyrene and dye (Fig. S11).

By further increasing the nanoparticles amount both the emission intensity and Φ_{scint} decrease significantly, thus suggesting that the 2.5%wt concentration is the maximum acceptable value before the nanoparticles starts to become competitive recombination

centres.[16, 20] The addition of nanoparticles only slightly modifies the light transport properties of the polymeric scintillator. From optical absorption experiments (Fig.2e) we estimate a scattering background as high as 0.15 of apparent absorbance for a 100 μm film with a 2.5%wt loading (Fig.2e), with no significant effect on the material light output.[21] Both the scintillation spectrum (Fig.2c) and kinetics (*vide infra*, Fig.5b) do not change in presence of nanoparticles, thus demonstrating that, when used with the correct amount, they act as perfectly passive scintillation sensitizers.[20a, 22] We speculate that the observed sensitization effect could be due to an enhanced conversion yield of the energy deposited by the ionizing radiation into emissive states upon both primary or secondary interaction with the dense particles. None clear explanation for this effect has been found in the literature, [23] and a dedicated study is still ongoing. It is worth noting that in this case Φ_{scint} is higher than for several commercial plastics, but also it matches the scintillation yield of BGO crystals (Φ_{scint}^{BGO}= 10000 ph MeV^{-1})[24] that will be used as dense component to fabricate the multilayer scintillating heterostructure. This will avoid any intrinsic unbalance in the generation of the scintillation photons, therefore making Eq. 2 valid also in the multilayer device.

As the fundamental building block of the multilayer device, a single heterostructure unit has been fabricated by coupling a 100 μm film of PS:POPOP-2.5%wt nanocomposite with a 100 μm thick BGO layer (Methods). Figures 2f shows the emission properties of the single heterostructure compared to the ones of the individual components. As depicted in Fig. S8, we studied the heterostructure in two configurations, by first exciting the BGO layer (configuration H1) and then by first exciting the composite layer (configuration H2). According to the low penetrability of soft X-rays in the dense component, by exciting the BGO layer the fast emitter cannot be activated nor directly neither by energy sharing, thus the scintillation emission spectrum matches the one of bulk BGO crystal (H1 spectrum). On the other hand, X-rays cannot be fully stopped by the plastic, so by hitting as first the fast emitter a fraction of X-rays can excite the BGO layer. Therefore, in this case the heterostructure emission spectrum is given by the convolution of PS:POPOP-2.5% and BGO (H2 spectrum). It should be noted that the UV tail of the BGO emission is partially reabsorbed by the composite in H1 and completely reabsorbed in H2 due to the filter effect of the composite layer (Fig.S8).

3. Observation of energy sharing in the multilayer scintillator.

The multilayer scintillating heterostructure has been realized by duplicating the heterostructure to reach a final size of 3×3×3 mm^3 (Methods). Figure 3a shows the pulse height spectra measured for the multilayer device compared to the one of a bulk BGO crystal and a bulk

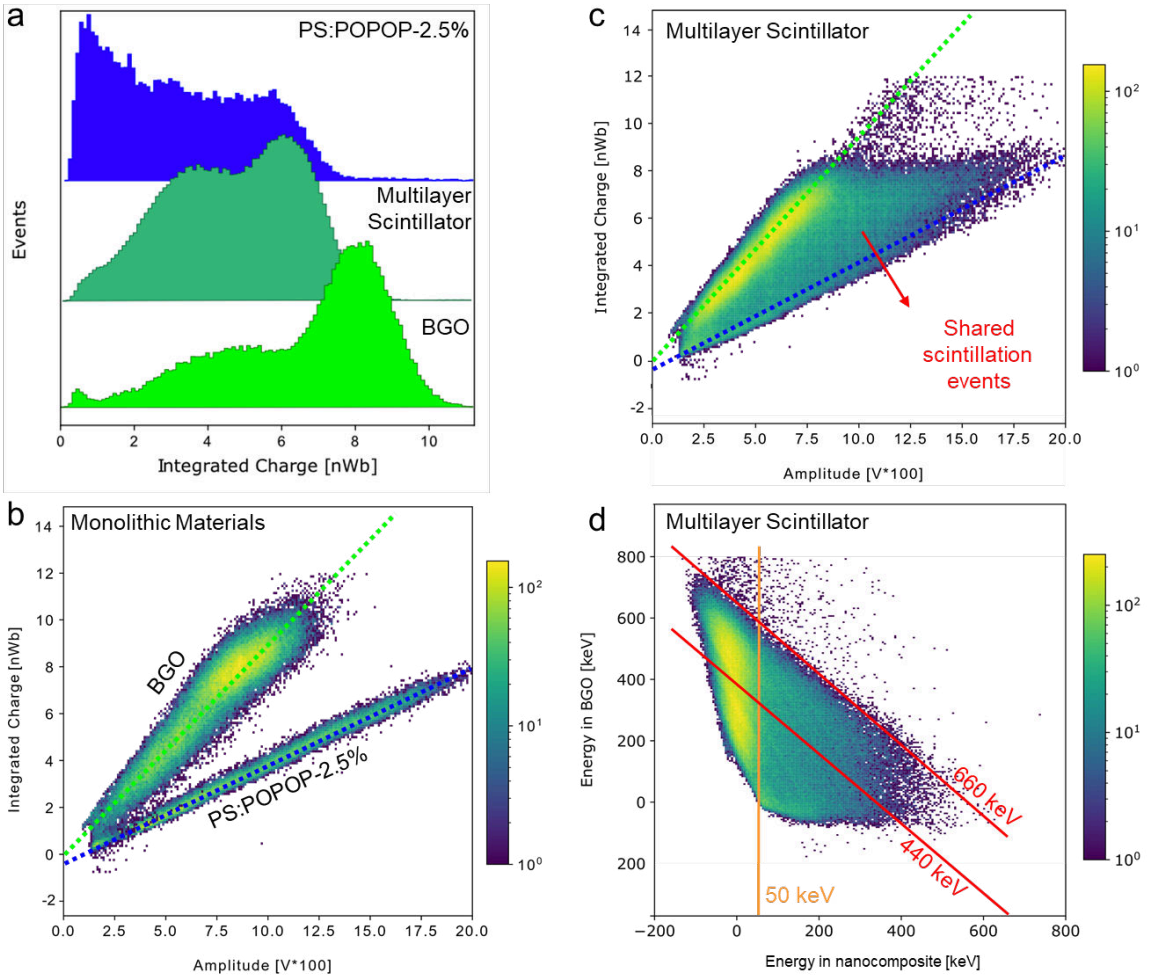

Figure 3. a) Pulse height spectrum of BGO, PS:POPOP-2.5% nanocomposite and the multilayer scintillator upon exposure to 511 keV γ-rays readout with a SiPM. b) Time integrated pulse-height spectra for bulk BGO overlapped to that one of monolithic PS:POPOP-2.5% composite. Dotted lines are a guide for the eye. c) Time integrated pulse-height spectrum of 3x3x3 mm^3 multilayer scintillator made alternating 100 mm layers of BGO and PS:POPOP-2.5%. Green and blue dotted straight lines are a guide for the eye to highlight the events occurring solely in BGO and nanocomposite, respectively, as like as in panel b. The shaded area between the straight lines marks the shared scintillation events. d) [energy in BGO] vs. [energy in nanocomposite] spectrum of the multilayer scintillator. Straight lines are the energy threshold values employed to select the shared fast scintillation events that originated from BGO photoelectric recoil electrons diffusing in the nanocomposite. As photoelectric events we consider those with total reconstructed deposited energy between 440 to 660 keV. We consider as shared photopeak only the events where at least 50 keV of energy is deposited in the nanocomposite by recoil electrons.

nanocomposite of the same size, under exposure to 511 keV γ-rays (Methods). The plot shows how the heterostructure spectrum has an intermediate behaviour compared to the one of BGO, where a clear photoelectric peak can be observed, and the one of the nanocomposite, where only the broad energy distribution due to the Compton effect appears. The pulse height spectrum of the multilayer still shows a photoelectric peak, but the ratio between photopeak and Compton events is lower due to the decreased photofraction of the heterostructure compared to bulk BGO (Supporting Table S4). Moreover, the photoelectric peak of the heterostructure is shifted toward lower values compared to bulk BGO because of the worse

light transport and collection in the multilayer vs. the monolithic device.[25] The correlation between the amplitude and time-integrated intensity of the scintillation energy signal of the different pulse shapes recorded was used to distinguish between events depositing energy in BGO, in the nanocomposite, or when the energy is shared.[25]

The time-integrated pulse height spectra for the reference samples is depicted in Fig.3b. Figure 3c shows the correlation between the amplitude and time-integrated intensity of the scintillation energy signal for each event. Because the nanocomposite and BGO have similar light output but the nominal emission lifetimes are 1.4 ns and 300 ns, respectively, the pulse shapes of events depositing energy in one or the other material are clearly different, thus allowing a clear pulse shape discrimination, as previously demonstrated. [24] [26] The multilayer scintillator shows a complex behaviour, with a spectrum that contains three regions of interest, as depicted in Fig.3c. The majority of events occur in the left-hand region marked with the green dotted line, where incoming photons interact with the heavy BGO and the recoil photoelectron is fully contained there (Fig.3b, top). The second region is in the lower part, marked with the blue dotted line, which point out the events that occur solely in the nanocomposite (Fig.3b, bottom). The triangular area between the two straight lines is attributed to the scintillation shared events described above, thus indicating that the global recorded output signal is not just the sum of two independent components but that there is an effective interaction between the different materials. According to Monte Carlo simulations of the radiation matter interaction in the system (Methods, Fig. S12), the average fraction of energy loss in the nanocomposite with respect to the total energy loss in the whole detector results as high as 0.35. This value is a net improvement with respect to the 0.29 predicted in a multilayer scintillator built using a pure polymeric fast scintillator, thus highlighting the role of HfO_2 nanoparticles in enhancing the stopping power of the polymeric component (Table S4). A more refined data analysis allows to distinguish the events useful for imaging reconstruction, i.e. the fast light pulses generated in the nanocomposite by recombination of the recoil electrons produced solely by photoelectric effect in the BGO. As shown in Fig.3d, the time resolved pulse height spectrum of the multilayer can be shown using smart coordinates change from the [time-integrated signal] vs [amplitude] to the [energy in BGO] vs. [energy in nanocomposite] system. This is done first by considering the peak corresponding to photoelectric events fully contained in BGO, as it is known to correspond to 511 keV energy deposited in BGO and 0 keV deposited in the nanocomposite. Then, the hypothetical photopeak in the nanocomposite, which would correspond to 0 keV deposited in BGO and 511 keV in the nanocomposite, can be reconstructed.[30] By knowing these two points, under the assumption of no saturation of the

SiPM, the energy calibration can be easily performed. The straight lines mark the region where we find the events where the total energy deposited in the device lies between 440 keV and 665 keV (24% of the total, Table S4) and at least 50 keV are shared in the nanocomposite. This energy window is the default setting employed in operating instrumentation, enabling the best performance for the image reconstruction by selecting with reasonable accuracy the 511 keV events, that is taken here as a reference operating condition.[25, 27]

4. Time resolution performance and scintillation kinetics.

The time resolution of the multilayer scintillator has been tested by means of ultrafast pulsed X-rays excitation and under exposure to 511 keV γ-rays. It is worth noting that the global distribution in time of scintillating pulses depends on several factors, such as the scintillation rise time and the effect of the device size and optical quality on the light propagation and photons paths, which set the pulses arrival time on the photodetector. Therefore, the reported data are specific of the considered sample series, where device geometry and instrumental setup have been fixed. As preliminary test, the detector time response has been measured under picoseconds X-ray pulsed excitation for the series of devices analysed (Methods).[28] As showed in **Figure 4a**, the bulk nanocomposite scintillation is significantly faster than the BGO, while the multilayer device shows the expected intermediate kinetics suggesting the simultaneous presence of fast, slow and energy shared-activated emission. The same is observed for the distribution in time of scintillations pulses rise time on the photodetector (Fig.4b). The intermediate behavior between the monolithic BGO and nanocomposite demonstrates again a synergistic global response of the two components in the device. Figure 4c reports the results of the CTR measurements. In detail, the CTR is obtained as the full width half maximum value of the statistical distribution of the recorded time differences in the detection of 511 keV back-to-back γ-rays emitted by ^{22}Na atoms (Methods).[26] The experiment has been performed on the whole scintillators series, and again the multilayer scintillator shows an intermediate behaviour with a good CTR of 180 ps that lies between the value of 244 ps for BGO and 141 ps for the bulk nanocomposite, respectively. Thanks to the energy sharing mechanism that activates the fast emission of the nanocomposite component, we successfully observe a clear improvement +26% of the device CTR with respect to bulk BGO, thus achieving a value close to the limit observed in the monolithic nanocomposite reference and very similar to what has been recently obtained using high density fast scintillators such as 2D-perovskite crystals.[9b] The same behaviour can be observed for the full width at tenth maximum (FWTM) of the scintillation events distribution, which together with the CTR sets the spatial resolution of the

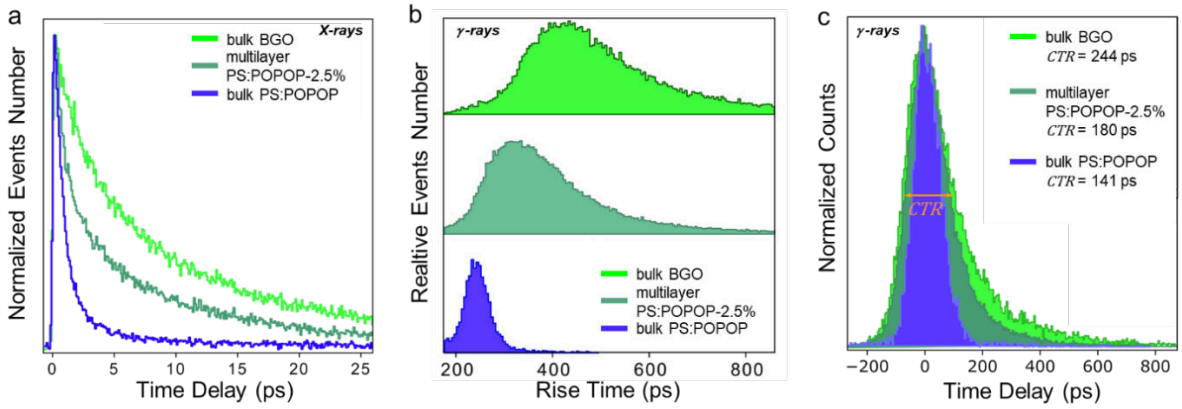

Figure 4. a, Detector time resolution measured under soft x-rays on in 3×3×3 mm^3 bulk BGO, monolithic PS:POPOP-2.5% nanocomposite and on the multilayer scintillator made alternating 100 μm layers of BGO and PS:POPOP-2.5% cubic heterostructure of size 3×3× mm^3. b, Distribution of the scintillation signal rise times on the photodetector measured for the BGO, PS:POPOP-2.5% composite and the multilayer scintillating heterostructure under 511 keV γ-rays exposure. c, Experimental CTR of bulk BGO, monolithic PS:POPOP-2.5% and the multilayer scintillating heterostructure measured under 511 keV γ-rays exposure.

ToF-PET image.[29] The FWTM of 418 ps of the heterostructure photopeak events distribution is indeed an intermediate value between the FWTM of the monolithic BGO (659 ps) and of the bulk nanocomposite (277 ps).

In order to shed light on which are the CTR limiting factors among the ones included in Eq.2, we investigated the intrinsic scintillation properties of its components. The multicomponent device global time response results actually as the linear combination of the single components' responses, weighted by the fraction of energy deposited in each one of them.[30] More in detail, we can reconstruct the global time response $CTR^{\dagger}$ by using

$$CTR^{\dagger} = 3.33\left(\frac{\tau_{rise}\,\bar{\tau}_{eff}}{\beta\chi[\Phi_{scint}E]}\right)^{0.5} = 3.33\sum_i A_i\left(\frac{\tau_{rise}\,\tau^i_{eff}}{\beta\chi[\Phi_{scint}E]}\right)^{0.5}, \qquad \text{Eq. 3}$$

where the device global scintillation decay time $\bar{\tau}_{eff}$ is given as the linear combination of all the possible τ^i_{eff} for each i-shared event. The τ^i_{eff} values depends on the effective scintillation decay time in the composite (τ^{nanoc}_{eff}) and in the BGO (τ^{BGO}_{eff}) by

$$\tau^i_{eff} = \left[\frac{\varepsilon_i}{\tau^{nanoc}_{eff}} + \frac{(1-\varepsilon_i)}{\tau^{BGO}_{eff}}\right]^{-1}. \qquad \text{Eq. 4}$$

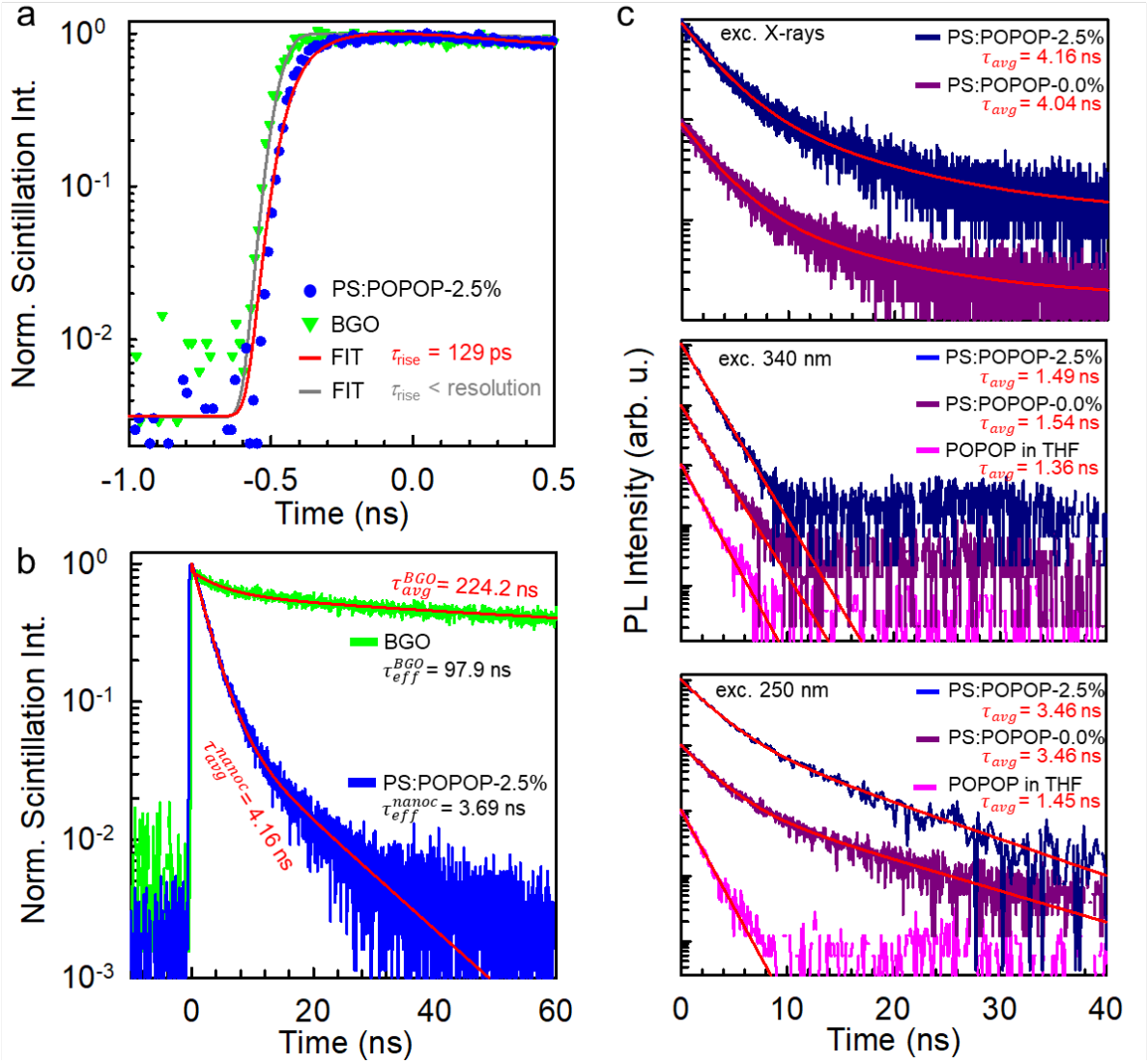

Figure 5. a, Rise time of the scintillation pulse measured for BGO and PS:POPOP-2.5% composite under ultrafast excitation with soft X-rays. Solid lines are the fit of the experimental data convoluted with the instrumental time response. b, Scintillation pulse decay in time under excitation with soft X-rays in BGO and PS:POPOP-2.5% nanocomposite. Solid lines are the fit with multi-exponential decay functions with characteristic average decay time τ_{avg}. The effective decay time reported τ_{eff} from the multi-exponential fit as described in the text. c. Top panel reports the luminescence decay in time at 420 nm recorded in PS:POPOP and PS:POPOP-2.5% composites under pulsed X-ray excitation. Middle and bottom panels show the luminescence decay in time recorded at 420 nm in PS:POPOP and PS:POPOP-2.5% vs. POPOP in tetrahydrofuran (THF) solution under pulsed laser excitation at 340 nm and 250 nm, respectively. The solid lines are the fit with single- or multi-exponential decay functions with characteristic average decay time τ_{avg}.

Their combination in Eq. 3 is weighted by the distribution of probability A_i that the i-shared event deposits in the nanocomposite a fraction ε_i of the BGO photoelectric recoil electrons energy (ε_i= energy deposited in the nanocomposite E_i / 511 k eV).

By directly measuring the properties of the individual materials, it is therefore possible to model the device $CTR^{\dagger}$ with good accuracy through Eqs. 3 and 4. Figure 5a shows the scintillation pulse rise kinetics measured in a BGO layer vs. the nanocomposite film. While for BGO the rise time is instantaneous, i.e. below the experimental resolution and therefore

negligible, the nanocomposite shows an intrinsic rise time as large as τ_{rise}^{0}=129 ps (Methods), which outperforms EJ-228™ (500 ps), EJ-230 ™ (500 ps), and EJ-232 ™ (350 ps) commercial scintillators. This value is in agreement with the estimated rate of the PS-to-POPOP energy transfer, and it should be used to calculate the global τ_{rise} as described above. Considering a device of size 3×3×3 mm^3 and scattering coefficient α_s = 0.232 cm^{-1} at 420 nm (Fig. 2f), we have a τ_{opt} = 85 ps given by the distribution of photons' optical paths before detection.[21] In this case, the combination of τ_{rise}^{0} and τ_{opt} results a device τ_{rise} as high as 298 ps. The effective scintillation decay time $\bar{\tau}_{eff}$ is calculated by combining scintillation experiments with Montecarlo simulations to evaluate the A_i and ε_i coefficients values, which are reported in the Supporting Table S5 (Methods and Supporting Information, section 7). Notably, the simulation results indicate that also the energy sharing effect is enhanced by the presence of nanoparticles with respect to a pure plastic scintillator, with a global increment of the fast scintillation emission by 20%. Figure 5b shows the scintillation pulses recorded for the BGO layer and for the nanocomposite film. Both materials show a multi-exponential decay of the emission intensity with time, from which we obtain a τ_{eff}^{BGO} = 97.9 ns and τ_{eff}^{nanoc}= 3.69 ns for the BGO and nanocomposite, respectively.[28, 31]

The theoretical best time response $CTR_{th}^{\dagger}$ can be now estimated as a function of the measured parameters, considering the certified χ = 0.5 at 420 nm for the photodetector and the ideal β = 0.65 for the selected experiment configuration (Methods).[21] The ideal $CTR_{th}^{\dagger}$ results as low as 94 ps. Considering that the only free parameter in Eq. 3 is the optical coupling factor β, we ascribe the difference with respect to the experimental result to a not ideal transport and extraction of photon within the scintillator to the photodetector. As suggested by the scintillation experiments discussed above (Fig.3a), the observed $CTR^{\dagger}$ value of 180 ps corresponds indeed to an effective low light outcoupling yield of β_{eff} = 0.2. This indicates that a large part of the scintillation photons is lost because of the device poor light transport properties, most probably due to the presence of many non-ideal interfaces between the layers composing the prototype.

Despite a non-optimized light transport/extraction, the time response of the multilayer scintillator is significantly improved with respect to the bulk and slow BGO scintillator, thanks to the highly efficient and fast scintillation achieved in the nanocomposite. However, we notice that the nanocomposite scintillation decay time is surprisingly longer than the POPOP intrinsic emission lifetime (Fig.5b). Indeed, while the BGO scintillation average decay time is 224.2 ns in agreement with literature values for both scintillation and photoluminescence,[28, 31] the

nanocomposite scintillation decays in 4.1 ns, i.e. more than twice than the POPOP photoluminescence. This means that, according to Eq. 3, the potential device time response is intrinsically worsened by a not negligible factor ~ 1.5. In order to understand the origin of this discrepancy, we investigated the nanocomposite scintillation and photoluminescence properties in parallel. Figure 5c shows the nanocomposite scintillation pulse decay measured in presence and absence of nanoparticles. No differences can be observed, thus demonstrating that nanoparticles do not affect the emission kinetics acting only as passive radiosensitizers. Interestingly, upon selective direct optical excitation of POPOP at 340 nm (Fig. S1), even if embedded in PS its emission decays in 1.4 ns, as like as a single molecule in solution and independently from the presence of nanoparticles (Fig.5c, mid panel). This also exclude potential effects of self-absorption on the excited states recombination kinetics. Conversely, the POPOP emission generated by energy transfer from the optically excited PS matrix at 250 nm, shows a clear increment in the emission lifetime up to 3.46 ns. This finding suggests therefore that the scintillation lifetime slowdown could depend on an interplay between the excited PS matrix and embedded POPOP molecules, affecting their radiative recombination rate. This picture is further supported by the fact that the energy transfer from PS-to-POPOP is fast enough to not affect the dye excited state recombination kinetics (Fig.S13). Moreover, trivial effects such as the reduction of intramolecular vibrational quenching upon embedding in PS can be excluded, because the POPOP has a photoluminescence quantum yield close to unity indicating the absence of this dispersion mechanism.[32] We speculate that the POPOP scintillation lifetime increment could be possibly due to local polarization of the excited matrix around the excited dyes,[32-33] or to the involvement of dark metastable states, which can act as intermediate energy reservoir, such as the polystyrene lowest energy triplet state T_1 at 388 nm that is strictly resonant with the dye S_0-S_1 transition at 380 nm eV (Fig. S1) or other types of defect and energetic traps in the host [32, 34]. A dedicated study is ongoing to elucidate this point, because it the observed slowdown of the emission can be dramatically detrimental in the search of the sub-nanosecond timing performance.

5. Conclusion

To summarize, we successfully fabricated a new fast emitting and high efficiency scintillating polymeric composite based on a polystyrene matrix loaded with scintillating conjugated dyes and high density nanoparticles to enhanced its stopping power. The loading level has been tuned to maximize the nanoparticle radiosensitization effect without introducing competitive

deactivation mechanisms. This allowed to increase the material scintillation yield by a factor 300%, surpassing several commercial plastic scintillators. The nanocomposite has been employed to fabricate a fast emitting multilayer scintillator as a prototype of the optical part of the detector that could be used in ToF-PET scanners for high-contrast fast imaging. The device has been realized by alternating nanocomposite films and crystalline BGO sheets as dense material to efficiently stop the ionizing radiation and activate the energy sharing mechanisms to trigger the fast nanocomposite emission. Upon exposure to γ-rays at 511 keV, we observe a synergistic response of the two components in the multilayer devices. Thanks to the effective activation of the nanocomposite fast emission upon energy sharing, we obtained a final coincidence time resolution of 180 ps, significantly better than for monolithic BGO (244 ps). The investigation of the scintillation process in the multicomponent device pointed out that its time response is limited by two main factors. The first one is the poor light transport and outcoupling of the scintillation photons. This can be straightforwardly improved by developing an accurate industrial manufacturing of the prototype device, still handmade. The second factor is more fundamental and deserve great attention. The analysis of the scintillation and luminescence processes in the nanocomposite suggest an unexpected interplay between the host matrix and the embedded dyes upon excitation at high energy. This mechanism, the origin of which is still to be clarified, result in a significant slowdown of the dyes luminescence decay rate by more than a factor of three, thus heavily affecting the time response of the device. This is a critical point that should be understood and managed to fully preserve the excellent fast emission properties of organic scintillators that can be exploited to achieve the desired time resolution below 50 ps for ToF-PET scanners.

As a final remark we would like to highlight that this study, which core is the development and engineering of a new nanocomposite having good light response, constitutes a general proof-of-concept strategy demonstration for device fabrication and performance investigation in the field of metascintillators. The CTR improvement obtained with this heterostructure is still not enough to compensate the lower sensitivity of bulk BGO at the level of reconstructed images. However, we successfully and systematically highlighted all the strong and weak points, in terms of scintillation speed, light transport, scintillation events distribution and fundamental photophysics, that should be faced to outperform the current ToF-PET technologies. Considering the good scintillation yield achieved in this first attempt of a global device development, future works will be focused to improve the time response and simultaneously increase the density of the nanocomposite. This strategy, together with a further

optimization of the scintillator architecture, [35] will finally allow to surpass the monolithic devices performances.

6. Methods

Preparation and structural characterization of HfO_2 nanoparticles. The HfO_2 nanoparticles were synthesized by hydrothermal route.[17] The standard experimental procedure is described as follows. The hafnium hydroxide chloride ($Hf(OH)_2Cl_2$) solution was firstly prepared by dissolving 0.160 g of $HfCl_4$ in 10.0 mL of deionized water. NaOH aqueous solution (3.0 M, 10.0 mL) was added dropwise to the solution above, causing the reaction with $Hf(OH)_2Cl_2$ to form hafnium hydroxide ($Hf(OH)_4$). After that, the solution was transferred into a 100 mL Teflon-lined autoclave and the sealed autoclave was heated to 120 °C and maintained for 72 hours. The products were purified by centrifugation for three cycles with alcohol and deionized water alternately after the autoclave was cooled down. Finally, the precipitate was dried at 50 °C for 24 hours. The structure and composition of HfO_2 nanoparticles were studied by means of powder X-ray diffraction (PXRD) structure refinement, Raman spectroscopy and transmission electron microscopy (TEM). Details and data are reported in the Supplementary Information file, section 2. XRD and Raman spectra show a well-defined series of diffraction peaks and Raman bands in good agreement with the values of monoclinic hafnium dioxide.[36],[37]

Preparation of polystyrene-based nanocomposites. Styrene monomer was purchased from Sigma-Aldrich (CAS no. 100-42-5) under the form of a liquid and colourless monomer. After the removal of stabilizer, the 1,4-Bis (5-phenyl-2-oxazolyl) benzene (POPOP, Sigma Aldrich, CAS no. 1806-34-4, MW=364.40 g/mol) dye was dissolved with the addition of the as-prepared hafnium oxide nanoparticles. Then, the monomer polymerization followed a thermal pathway by using Azobisisobutyronitrile (AIBN), a free radical initiator, the VAZO™ 64 (Chemours™). The final composition was obtained as follows: 3.64 mg of POPOP and 1 mg of VAZO™ 64 were dissolved in 1 ml of styrene through ultrasonic stirring. Then 25±1 mg of hafnium oxide nanoparticles were added to the solution, and then dispersed through stirring. The as-prepared solution was placed in a temperature-controlled oil bath at 80°C for 1 day. For the first 8 hours, the mixture was mechanically stirred every hour to avoid nanoparticles sedimentation. At the end of the process, we obtained a polystyrene-based plastic scintillator with a 10^{-2} M dye concentration and 2.5+0.1% wt hafnium oxide nanoparticles loading.

Preparation of nanocomposites films. 100 μm polystyrene films loaded with 10^{-2} M 1,4-Bis (5-phenyl-2-oxazolyl) benzene and 2.5% wt of hafnium oxide nanoparticles were prepared as follows: 1g of composite prepared as discussed in the section above was dissolved in 1 ml of DCM (Sigma Aldrich, CAS no. 75-09-2). Once the solution reached a syrup-like viscosity it was deposited with the help of a doctor blade using a 5 mils blade. The film was then left air drying until the complete solvent evaporation.

Assembling of scintillating heterostructures. The 3×3×0.1 mm^3 BGO sheets, purchased from EPIC Crystal LTD, and 0.1 mm nanocomposite films were assembled together by hand using un-polymerized styrene monomer as a glue, realising an ultra-thin layer acting as adhesive for the composite films. Once the latter sheet has been placed in position, the whole heterostructure was left under chemical hood for the monomer to self-polymerize. For more accurate measurements and to maximize the device quality, the multilayer scintillator has been fabricated by alternating BGO and nanocomposite 0.1 mm layers, with no glue, in a custom

made sample holder, specifically a 3×3×3 mm^3 Teflon cube with one face open, which internal surface has been covered by ESR (Vikuiti) form 3M as reflecting material.

Photoluminescence studies. Time-resolved photoluminescence experiments in the nanosecond time scale have been performed by using as excitation source a pulsed laser LED at 340 nm (3.65 eV, EP-LED 340 Edinburgh Instruments, pulse width 120 ps) and a pulsed laser LED at 250 nm (4.95 eV, EP-LED 250 Edinburgh Instruments, pulse width 77 ps) coupled to FLS980 Edinburgh setup in Time-Correlated Single Photon Counting (TCSPC) acquisition mode. Quartz Suprasil cuvettes with 1 cm of optical path has been used for all the experiments listed above to study dyes solution. The nanocomposites were excited with a pulsed laser at 340 nm avoiding the excitation of the polystyrenic matrix, coupled to FLS980 Edinburgh setup in Time-Correlated Single Photon Counting (TCSPC) acquisition mode.

Radioluminescence studies. Steady state RL measurements were carried out at room temperature using a homemade apparatus featuring, as a detection system, a liquid nitrogen-cooled, back-illuminated, and UV-enhanced charge coupled device (CCD) Jobin-Yvon Symphony II, combined with a monochromator Jobin-Yvon Triax 180 equipped with a 100 lines/mm grating. All spectra are corrected for the spectral response of the detection system. RL excitation was obtained by unfiltered X-ray irradiation through a Be window, using a Philips 2274 X-ray tube with tungsten target operated at 20 kV. At this operating voltage, a continuous X-ray spectrum is produced by a Bremsstrahlung mechanism superimposed to the L and M transition lines of tungsten, due to the impact of electrons generated through thermionic effect and accelerated onto a tungsten target. The dose rate was 5 mGy/ s, evaluated with an ionization chamber in air. The nanocomposites Φ_{scint} has been measured my relative methods using the EJ-276 (Φ_{scint} = 8600 ph MeV^{-1}) plastic scintillator as reference.

X-rays scintillation. The scintillation emission rate was studied in time correlated single photon counting (TCSPC) mode under pulsed X-ray excitation. For this purpose, X-ray Tube (XRT) N5084 of Hamamatsu was used. The X-rays energy spectrum is a bremsstrahlung continuous spectrum extending up to 40 keV (as the operating voltage is 40kV, pulse width 80 ps) with an additional pronounced peak around 9keV due to Tungsten L-characteristic X-ray photons. As photodetector. As photodetector, a hybrid photomultiplier tube (HPM 100-07 from Becker&Hickl) optimized for TCSPC measurement was used. The samples were measured in anti-reflection positioning. [28] The scintillation emission rates were fitted with the convolution between the overall instrument response function (IRF) of the system and the intrinsic scintillation rate. The former was obtained by the analytical convolution between the measured IRF of the laser together with HPM and the IRF of the X-ray tube resulting around 110 ps FWHM. The latter was modelled with a sum of bi-exponential functions.

Detector Time Resolution (DTR) measurements. The excitation branch of the system is the same as for scintillation decay measurements, the difference is in the detector. Here a SiPM (from Hamamatsu, 53 V breakdown voltage, 61 V bias voltage) is used, its signal is split in two in order to optimise independently the energy and time information. The first one is processed by an analog amplifier, while the latter by a custom made high-frequency amplifier (two cascade radio frequency BGA616 amplifiers).[26] The outputs are then digitized at the oscilloscope (Lecroy, WaveRunner 8104, 20 Gs/s sample rate, 1 GHz bandwidth), where all information required for the analysis is measured and extracted directly from the waveforms. The samples were wrapped with one layer of Teflon positioning them on the SiPM without applying any glue or grease for the optical coupling.[28]

CTR measurements. The CTR under 511keV was measured with a standard setup as previously described.[26] In brief, a ^{22}Na radioactive source emits two back-to-back 511 keV gamma photons which are detected by two detectors in coincidence. On one side a reference crystal (LSO:Ce:Ca0.4% 2x2x3 mm^3, 61ps CTR FWHM), on the other side the sample under investigation (BGO 3x3x3 mm^3, POPOP:HfO_2 3×3×3 mm^3, heterostructure BGO+POPOP:HfO_2 3×3×3 mm^3). Both samples are coupled to a SiPM through Meltmount glue (1.58 refractive index), mounted perpendicularly to the multilayer structure. For the samples under investigation was a Hamamatsu SiPM (53 V breakdown voltage, 61 V bias voltage) was used. The readout electronics was the same used also for DTR measurements. The output signals feed an oscilloscope (LeCroy DDA735Zi oscilloscope with 3.5 GHz bandwidth and a sampling rate of 40 Gs s^{-1}), where all information required for the analysis is measured and extracted directly from the waveforms.

Monte Carlo Simulations. In order to evaluate the expected energy sharing between the slow BGO crystal and fast scintillator component, a Monte Carlo simulation of the experimental setup has been performed by means of the FLUKA code.[38] The geometry of the multilayer scintillating heterostructure with a final size of 3×3×3 mm^3, as well as the two components materials (BGO and POPOP:HfO_2), in terms of atomic weights and density, have been fully reproduced. A 511 keV photon isotropic source has been simulated, at a distance of 0.5 cm from the detector surface. Dedicated user-routines have been developed in order to analyse the simulation output on an event-by-event basis, providing the information of the energy deposits in the detector. No optical simulation has been performed at this stage.

*Scintillation pulse simulation*s. Scintillation pulse simulations and fitting have been performed considering deconvolution of Instrument Response Function (IRF) with rise and decay times. The temporal profile of scintillation can be described as:

$$I(t) = (f * g)(t) \coloneqq \int_0^t f(\tau)\, g(t-\tau) d\tau$$

Where f(t) and g(t) represent the IRF and a combination of rise and decay functions, respectively. The temporal profile of IRF has been assumed to be Gaussian in shape:

$$f(t) = \frac{e^{-\frac{(t-t_0)^2}{2{w_t}^2}}}{\sqrt{2\pi} w_t}$$

Where t_0 and w_t are the temporal position of the peak maximum and the standard deviation of the IRF. The latter includes the duration of both the x-ray excitation and the detector response. In our apparatus, the FWHM of the IRF is equal to 110 ps corresponding to a deviation standard $w_t \approx$ FWHM/2.35=47 ps.

The time decay of the sample has been modelled as the product of a rising exponential and a decaying exponential:

$$g(t) = \left(1 - e^{-\frac{t}{\tau_R}}\right) e^{-\frac{t}{\tau_D}}$$

Considering the definitions of *f(t)* and *g(t)*, the convoluted signal can be represented as:

$$I(t) = \int_0^t f(\tau)\, g(t-\tau) d\tau = \int_0^t \frac{e^{-\frac{(\tau - t_0)^2}{2{w_t}^2}}}{\sqrt{2\pi} w_t} \left(1 - e^{-\frac{(t-\tau)}{\tau_R}}\right) e^{-\frac{(t-\tau)}{\tau_D}} d\tau$$

Which has the following analytical solution:

$$I(t) = c + \frac{1}{2} e^{\frac{{w_t}^2 + 2\tau_D(t_0 - t)}{2{\tau_D}^2}} \left(\mathrm{Erf}\left[\frac{{w_t}^2 + t_0\tau_D}{\sqrt{2} w_t \tau_D}\right] - \mathrm{Erf}\left[\frac{{w_t}^2 + (t_0 - t)\tau_D}{\sqrt{2} w_t \tau_D}\right]\right) +$$
$$+ \frac{1}{2} e^{\frac{(\tau_D + \tau_R)[2(t_0 - t)\tau_D\tau_R + {w_t}^2(\tau_D + \tau_R)]}{2{\tau_D}^2{\tau_R}^2}} \left(\mathrm{Erf}\left[\frac{(t_0 - t)\tau_D\tau_R + {w_t}^2(\tau_D + \tau_R)}{\sqrt{2} w_t \tau_D \tau_R}\right] - \mathrm{Erf}\left[\frac{t_0\tau_D\tau_R + {w_t}^2(\tau_D + \tau_R)}{\sqrt{2} w_t \tau_D \tau_R}\right]\right)$$

Where t_0 and w_t are known and define the IRF shape. The parameters used to fit normalized scintillation pulse data are c, τ_R, and τ_D which represent the constant dark background, and the rise and the decay constants, respectively. Simulations, reported in Fig. S13, have been calculated assuming $c=0$, $t_0=0.5$ *ns* and $w_t = 47$ *ps*, keeping fix τ_D at 1.5 ns, and varying τ_R from 10 ps to 10 ns. The fitting procedure reliability has been validated by looking at the adjusted R-squared calculated for the scintillation pulses fit function, which are corrected by the degrees of freedom. We have an adjusted R square of 0.997953 and of 0.998566 for the BGO pulse and for the PS:POPOP-2.5% pulse, respectively.

Supporting Information

Supporting Information is available from the Wiley Online Library or from the author.

Data Availability.

All data are available from the authors upon reasonable request.

Acknowledgements

This work was carried out in the framework of Crystal Clear Collaboration. We acknowledge support from the European Community through the grant no. 899293, HORIZON 2020 - SPARTE FET OPEN. Financial support from the Italian Ministry of University (MUR) through grant no. PRIN 2020—SHERPA no. H45F2100343000. CERN knowledge transfer for medical applications budget. Cranfield University, acknowledges that part of this research was funded by the UK Engineering and Physical Sciences Research Council (EPSRC) grant EP/S013652/1. We thank Professor Anna Vedda, for valuable discussions.

References

[1] a)M. Conti, B. Bendriem, *Clinical and Translational Imaging* **2019**, 7, 139; b)D. R. Schaart, *Physics in Medicine & Biology* **2021**, 66, 09TR01.

[2] E. Auffray, B. Frisch, F. Geraci, A. Ghezzi, S. Gundacker, H. Hillemanns, P. Jarron, T. Meyer, M. Paganoni, K. Pauwels, M. Pizzichemi, P. Lecoq, presented at *2011 IEEE Nuclear Science Symposium Conference Record*, 23-29 Oct. 2011, **2011**.

[3] a)S. Vinogradov, *Nuclear Instruments and Methods in Physics Research Section A: Accelerators, Spectrometers, Detectors and Associated Equipment* **2018**, 912, 149; b)E. Auffray, B. Frisch, F. Geraci, A. Ghezzi, S. Gundacker, H. Hillemanns, P. Jarron, T. Meyer, M. Paganoni, K. Pauwels, M. Pizzichemi, P. Lecoq, *IEEE Transactions on Nuclear Science* **2013**, 60, 3163.

[4] M. Conti, *Physica Medica* **2009**, 25, 1.

[5] J. S. Reddin, J. S. Scheuermann, D. Bharkhada, A. M. Smith, M. E. Casey, M. Conti, J. S. Karp, presented at *2018 Ieee nuclear science symposium and medical imaging conference proceedings (Nss/Mic)*, **2018**.

[6] P. Lecoq, C. Morel, J. O. Prior, D. Visvikis, S. Gundacker, E. Auffray, P. Križan, R. M. Turtos, D. Thers, E. Charbon, J. Varela, C. de La Taille, A. Rivetti, D. Breton, J.-F. Pratte, J. Nuyts, S. Surti, S. Vandenberghe, P. Marsden, K. Parodi, J. M. Benlloch, M. Benoit, *Physics in Medicine & Biology* **2020**, 65, 21RM01.

[7] M. J. Weber, *Journal of Luminescence* **2002**, 100, 35.

[8] B. Bengtson, M. Moszynski, *Nuclear Instruments and Methods* **1978**, 155, 221.

[9] a)R. M. Turtos, S. Gundacker, E. Auffray, P. Lecoq, *Physics in Medicine & Biology* **2019**, 64, 185018; b)E. G. Rogers, M. D. Birowosuto, F. Maddalena, C. Dujardin, F. Pagano, N. Kratochwil, E. Auffray, P. Krause, G. Bizarri, *Applied Physics Letters* **2023**, 122.

[10] P. Lecoq. *Nuclear Instruments and Methods in Physics Research Section A: Accelerators, Spectrometers, Detectors and Associated Equipment* **2016**, 809, 130-139

[11] O. Kilicoglu, E. E. Altunsoy, O. Agar, M. Kamislioglu, M. I. Sayyed, H. O. Tekin, N. Tarhan, *Results in Physics* **2019**, 14, 102424.

[12] S. Berns, A. Boyarintsev, S. Hugon, U. Kose, D. Sgalaberna, A. D. Roeck, A. Lebedynskiy, T. Sibilieva, P. Zhmurin, *Journal of Instrumentation* **2020**, 15, P10019.

[13] G. H. Bertrand, M. Hamel, S. Normand, F. Sguerra, *Nuclear Instruments and Methods in Physics Research Section A: Accelerators, Spectrometers, Detectors and Associated Equipment* **2015**, 776, 114.

[14] a)C. Liu, T. J. Hajagos, D. Kishpaugh, Y. Jin, W. Hu, Q. Chen, Q. Pei, *Advanced Functional Materials* **2015**, 25, 4607; b)I. Villa, F. Moretti, M. Fasoli, A. Rossi, B. Hattendorf, C. Dujardin, M. Niederberger, A. Vedda, A. Lauria, *Advanced Optical Materials* **2020**, 8, 1901348.

[15] a)I. B. Berlman, *Handbook of fluorescence spectra of aromatic molecules*, Academic Press, New York **1971**; b)P. Smith, P. Liao, C. Shank, C. Lin, P. Maloney, *IEEE Journal of Quantum Electronics* **1975**, 11, 84.

[16] T. J. Hajagos, C. Liu, N. J. Cherepy, Q. Pei, *Advanced Materials* **2018**, 30, 1706956.

[17] Y. Wan, X. Zhou, *RSC Advances* **2017**, 7, 7763.

[18] A.-L. Bulin, A. Vasil'ev, A. Belsky, D. Amans, G. Ledoux, C. Dujardin, *Nanoscale* **2015**, 7, 5744.

[19] I. Villa, A. Lauria, F. Moretti, M. Fasoli, C. Dujardin, M. Niederberger, A. Vedda, *Physical Chemistry Chemical Physics* **2018**, 20, 15907.

[20] a)I. Villa, B. Santiago Gonzalez, M. Orfano, F. Cova, V. Secchi, C. Colombo, J. Páterek, R. Kučerková, V. Babin, M. Mauri, M. Nikl, A. Monguzzi, *Nanomaterials* **2021**, 11, 3387; b)K. Rajakrishna, A. Dhanasekaran, N. Yuvaraj, K. C. Ajoy, B.

Venkatraman, M. T. Jose, *Nuclear Instruments and Methods in Physics Research Section A: Accelerators, Spectrometers, Detectors and Associated Equipment* **2021**, 1008, 165454.
[21] J. Perego, I. Villa, A. Pedrini, E. C. Padovani, R. Crapanzano, A. Vedda, C. Dujardin, C. X. Bezuidenhout, S. Bracco, P. E. Sozzani, A. Comotti, L. Gironi, M. Beretta, M. Salomoni, N. Kratochwil, S. Gundacker, E. Auffray, F. Meinardi, A. Monguzzi, *Nature Photonics* **2021**, 15, 393.
[22] a)T. L. McGinnity, O. Dominguez, T. E. Curtis, P. D. Nallathamby, A. J. Hoffman, R. K. Roeder, *Nanoscale* **2016**, 8, 13627; b)T. J. Hajagos, C. Liu, N. J. Cherepy, Q. Pei, *Advanced Materials* **2018**, 30, 1706956.
[23] T. M. Demkiv, O. O. Halyatkin, V. V. Vistovskyy, V. B. Hevyk, P. M. Yakibchuk, A. V. Gektin, A. S. Voloshinovskii, *Nuclear Instruments and Methods in Physics Research Section A: Accelerators, Spectrometers, Detectors and Associated Equipment* **2017**, 847, 47.
[24] M. Kapusta, J. Pawelke, M. Moszyński, *Nuclear Instruments and Methods in Physics Research Section A: Accelerators, Spectrometers, Detectors and Associated Equipment* **1998**, 404, 413.
[25] F. Pagano, N. Kratochwil, M. Salomoni, M. Pizzichemi, M. Paganoni, E. Auffray, *Physics in Medicine & Biology* **2022**, 67, 135010.
[26] S. Gundacker, R. M. Turtos, E. Auffray, M. Paganoni, P. Lecoq, *Physics in Medicine & Biology* **2019**, 64, 055012.
[27] S. Surti, A. Kuhn, M. E. Werner, A. E. Perkins, J. Kolthammer, J. S. Karp, *Journal of Nuclear Medicine* **2007**, 48, 471.
[28] F. Pagano, N. Kratochwil, I. Frank, S. Gundacker, M. Paganoni, M. Pizzichemi, M. Salomoni, E. Auffray, *Frontiers in Physics* **2022**, 10.
[29] C. Desmonts, C. Lasnon, C. Jaudet, N. Aide, *EJNMMI Physics* **2023**, 10, 61.
[30] F. Pagano, N. Kratochwil, L. Martinazzoli, C. Lowis, M. Paganoni, M. Pizzichemi, E. Auffray, *IEEE Transactions on Nuclear Science*, doi: 10.1109/TNS.2023.3332699.
[31] a)M. Ishii, K. Harada, Y. Hirose, N. Senguttuvan, M. Kobayashi, I. Yamaga, H. Ueno, K. Miwa, F. Shiji, F. Yiting, M. Nikl, X. Q. Feng, *Optical Materials* **2002**, 19, 201; b)R. Cala', N. Kratochwil, L. Martinazzoli, M. T. Lucchini, S. Gundacker, E. Galenin, I. Gerasymov, O. Sidletskiy, M. Nikl, E. Auffray, *Nuclear Instruments and Methods in Physics Research Section A: Accelerators, Spectrometers, Detectors and Associated Equipment* **2022**, 1032, 166527.
[32] J. B. Birks, *Photophysics of aromatic molecules*, Wiley-Interscience, London **1970**.
[33] M. Baruah, W. Qin, C. Flors, J. Hofkens, R. A. Vallée, D. Beljonne, M. Van der Auweraer, W. M. De Borggraeve, N. Boens, *J. Phys. Chem. A* **2006**, 110, 5998.
[34] a)S. Tagawa, N. Nakashima, K. J. M. Yoshihara, **1984**, 17, 1167; b)S. Reineke, M. Baldo *Scientific Reports* **2014**, 4, 3797.
[35] P. Krause, E. Rogers, G. Bizarri, Advances in Design of High-Performance Heterostructured Scintillators for Time-of-Flight Positron Emission Tomography. *Adv. Theory Simul.* **2023**, 7, 2300425.
[36] A. Ramadoss, K. Krishnamoorthy, S. J. Kim, *Materials Research Bulletin* **2012**, 47, 2680.
[37] I. Villa, A. Vedda, M. Fasoli, R. Lorenzi, N. Kränzlin, F. Rechberger, G. Ilari, D. Primc, B. Hattendorf, F. J. Heiligtag, M. Niederberger, A. Lauria, *Chemistry of Materials* **2016**, 28, 3245.
[38] a)A. Ferrari, J. Ranft, P. R. Sala, A. Fassò, *FLUKA: A multi-particle transport code (Program version 2005)*, Cern, **2005**; b)T. T. Böhlen, F. Cerutti, M. P. W. Chin, A. Fassò, A. Ferrari, P. G. Ortega, A. Mairani, P. R. Sala, G. Smirnov, V. Vlachoudis, *Nuclear Data Sheets* **2014**, 120, 211.

https://dspace.org/

Fast emitting nanocomposites for high-resolution ToF-PET imaging based on multicomponent scintillators

Orfano, Matteo; Pagano, Fiammetta; Mattei, Ilaria; Cova, Francesca; Secchi, Valeria ...

2024-05-22
Wiley
https://doi.org/10.1002/admt.202302075
Orfano M, Pagano F, Mattei I, et al., (2024) Fast Emitting Nanocomposites for High Resolution ToFPET Imaging Based on Multicomponent Scintillators. Advanced Materials Technologies, Volume 9, Issue 10, May 2024, Article number 2302075

Downloaded from a DSpace repository. https://dspace.org/